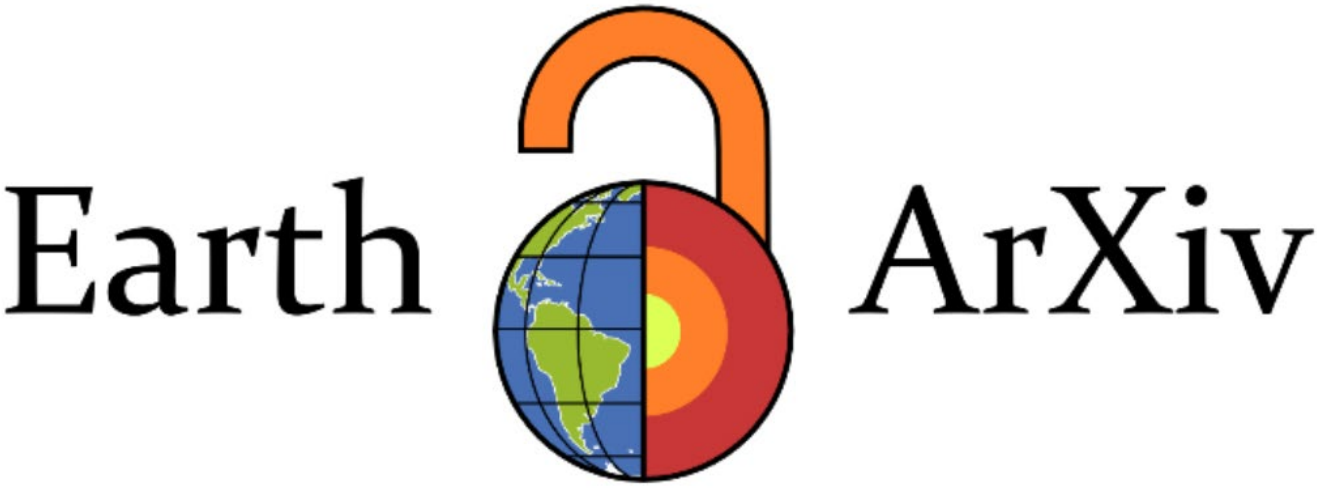

Peer review status:
This is a non-peer-reviewed preprint submitted to EarthArXiv

Large-Scale Mapping and Graph-Theoretic Characterization of Arctic Tundra Capillary Networks From Submeter Satellite Imagery

Michael Pimenta[1], Chandi Witharana[1], Amal Perera[1], Anna K. Liljedahl[2]

***Abstract*— Tundra capillary networks (TCNs) are visible surface-drainage features associated with ice-wedge polygon terrain that can influence lateral surface-water redistribution across Arctic landscapes. However, TCN systems remain poorly characterized at regional scales because their narrow morphology, variable surface expression, and submeter scale have limited the development of scalable mapping and characterization methods. To address this gap, we present the first scalable GeoAI segmentation-to-graph framework for regional mapping and structural characterization of visible TCN expressions directly from very high spatial resolution satellite imagery. Using the first labeled remote-sensing dataset developed specifically for TCN segmentation, we implemented a systematic model-development workflow comparing convolutional neural network and transformer-based architectures across four spatial-context configurations and tuned SegFormer MiT-b3 with 1024 x 1024-pixel inputs as the highest-performing model (F1 = 0.89). Independent assessment at three Alaskan sites produced F1-scores ranging from 0.80 to 0.93, demonstrating transferability across diverse tundra landscapes. The selected model was deployed across a 728,400 km² northern Alaska WorldView-2/3 mosaic composed of 1,821 20 × 20-km sub-grid cells. The workflow mapped approximately 2.7 million km of TCN centerlines and converted the resulting detections into graph representations describing nodes, edges, connected components, and network extent. The resulting products provide the first regional baseline for characterizing the distribution and structural variability of visible TCN expressions across northern Alaska. Our framework demonstrates how submeter satellite imagery, deep learning, and graph theory can be combined to transform large Earth-observation archives into interpretable regional-scale products for Arctic landscape analysis.**

***Index Terms*—**Remote Sensing, Deep Learning, Vision Transformers, Arctic Permafrost, Tundra, GeoAI, Graph Theory, Image Segmentation, Tundra Hydrology, Very High Spatial Resolution Imagery

This research was supported by the Google.org's Impact challenge on Climate Innovation grant, U.S. National Science Foundation (NSF) grant #: 1720875, 1722572, 1927872, 1927723, 1927729. eXtreme Science and Engineering Discovery Environment (Award #: DPP 190001) and Texas Advanced Computing Center Award #: DPP 20001). Authors would like to thank the Polar Geospatial Center, University of Minnesota for imagery support under NSF-OPP awards: # 1043681 and 1559691 .

[1]Department of Natural Resources and the Environment, University of Connecticut, 1376 Storrs Road, Unit 4087, Storrs, CT 06269, USA michael.pimenta@uconn.edu, chandi.witharana@uconn.edu, amal.perera@uconn.edu.

[2]Woodwell Climate Research Center, 149 Woods Hole Road, Falmouth, MA 02540, USA. aliljedahl@woodwell.org.

I. INTRODUCTION

The Arctic has warmed nearly four times faster than the global average since 1979, driving widespread changes across permafrost landscapes [1], [2]. Permafrost, ground that remains at or below 0°C for at least two consecutive years, underlies 15% of the Northern Hemisphere's exposed land surface [3], [4]. However, these landscapes vary considerably in ground-ice content, hydrology, vegetation, biogeochemistry, geologic history, and local climatic conditions [5], [6]. Consequently, this heterogeneity means permafrost thaw does not produce a uniform landscape-scale response across the Arctic [7].

Ice-rich permafrost landscapes are commonly patterned by ice-wedge polygons (IWPs) [8]. IWPs develop as repeated freeze-thaw contraction cracking allow for wedge-shaped ice bodies to grow beneath the surface [9], [10]. The surface expression consists of polygon centers that are bordered by rims and trough depressions, with the relative elevation of these features varying across stages of development and degradation [11]. Troughs are especially important for describing this system's function as they act as depressional pathways for surface water to travel across landscapes [2]. As this system further degrades, troughs can deepen and connect, reorganizing local drainage [2].

Building upon the concept of tundra capillaries introduced by Liljedahl et al. [12], this study formally defines tundra capillary networks (TCNs) for remote sensing-based modelling. TCNs are visible surface drainage features associated with the progressive degradation, deepening, and coalescence of ice-wedge polygon troughs [2], [12]. They encompass both isolated trough-like segments and larger interconnected networks, reflecting the progressive organization of these features across the landscape. This definition consolidates features historically described using varied terminology for ice-wedge polygon trough systems. Importantly, because TCNs are delineated from satellite imagery, the term refers to their visible surface expression rather than field-verified trough morphology. Because TCNs influence lateral surface-water redistribution, their spatial organization provides a remotely observable link between permafrost-degradation-driven microtopographic change, and surficial hydrological response [2], [12].

Previous efforts to map and analyze IWP and TCN systems have relied on field surveys, manual digitization of the feature, digital elevation models (DEMs) and semi-automated methods

including object-based image analysis [2], [13], [14]. Field-based approaches to studying these systems provide high-quality observations essential for understanding these systems better. Despite this, field-based approaches remain spatially limited due to cost and logistics limiting their ability to characterize landscape variability beyond sampled locations [15]. Manual digitization can produce high-quality delineations of IWPs and TCNs, however the process is time- and labor-intensive making large scale analysis impractical [15]. Very high-resolution elevation data has demonstrated promising potential in analysis of these systems; however, these datasets are spatially limited across the Arctic [13], [14]. Other, coarser elevation products often lack the spatial resolution necessary to resolve narrow features including TCNs [13], [14], [15]. Semi-automated methods, including object-based image analysis, can reduce the manual effort required, but their reliance on site-specific adjustments and analyst-defined rules and thresholds can limit their transferability across large heterogeneous regions [15]. Consequently, no fully automated, generalizable, and scalable framework currently exists to map TCNs and quantify their network structure across landscape-scale extents.

The rapidly growing availability of very high spatial resolution (VHSR) satellite imagery provides new opportunities to map TCNs directly from the visible surface expression [15]. Commercial satellite imagery providers, such as Vantor with WorldView data, can resolve sub-meter TCN expressions across varying space and time [15], [16]. Despite the great potential, the size and complexity of these archives make manual interpretation infeasible at scale [15]. TCN feature detection is further complicated by extreme variability in their surface expressions. TCNs may be water-filled, vegetated, dry, or weakly expressed depending on environmental conditions, image acquisition timing, and degradation state [15], [17].

Recent advancements in deep learning-based computer vision provide a promising approach for autonomous detection of subtle geomorphologic features directly from VHSR satellite imagery [18], [19]. However, direct application of these models remains challenging as TCNs are narrow, spatially continuous, and sometimes weakly expressed within heterogeneous tundra landscapes [2], [12], [15]. Their detection depends not only on local spectral and textural signals, but also on their relationship to the surrounding IWP-patterned terrain [15]. Input tile size, or the spatial extent of the imagery provided to the model during training and inference, therefore represents a key consideration for modelling efforts [20], [21]. Smaller tiles can highlight the relative prominence of narrow features but consequently may also provide insufficient context for the model [20], [21]. Larger tiles provide greater spatial context but increase the computational demand of model training and deployment, introduce more background complexity, and proportionally reduce the representation of the target TCN class within each tile. These larger contextual windows may also require more diverse datasets to support reliable learning [20], [21]. Model architecture and encoder configuration introduce further considerations as the ability to extract fine-scale features while also representing broader spatial relationships may vary substantially across different configurations [21]. A systematic evaluation of architecture, encoder, and input tile size configuration is therefore necessary to develop a highly effective modelling framework for TCN detection across heterogeneous Arctic tundra landscape regions.

Autonomous detection alone is insufficient for characterizing TCNs as landscape-scale systems. Computer vision-based segmentation can identify where visible expressions occur, but it cannot describe whether the mapped features form isolated segments or larger interconnected drainage networks. Graph theory provides an efficient framework for describing and quantifying the structural organization of spatial networks [13], [22], [23]. By converting mapped TCN features into simplified graph-based representations, patterns in connectivity, fragmentation, and extent, can be evaluated at landscape-scale [13]. Deep learning-based segmentation-to-graph frameworks remain rare and have not yet been developed for TCNs, leaving their networks largely unquantified. To our knowledge, no scalable remote sensing-based framework currently exists to map TCNs and characterize their graph-theoretic structure across landscape-scale extents.

To address prevailing methodological gaps, this study develops a task-specific, scalable remote sensing-based framework combining deep learning–based image segmentation with graph-theoretic modelling to systematically quantify and characterize TCN structure. We first performed an ablation study to evaluate multiple deep learning architectures, encoder configurations, and input tile sizes configurations to develop a highly effective approach for TCN segmentation. We then assess the spatial generalizability of the best-performing design configuration across multiple Alaskan sites. Finally, the developed segmentation-to-graph framework is deployed across a northern Alaska satellite imagery mosaic to produce a regional-scale baseline characterization of TCN distribution and variability.

II. METHODS

A. GeoAI Framework

The GeoAI framework used in this study is summarized in Fig. 3. The workflow integrates four linked stages: spatial-context modeling through systematic evaluation of input tile size, architecture, and encoder configuration; image segmentation using the selected model to produce georeferenced TCN detection masks; graph construction through mask refinement, vector extraction, skeletonization, and conversion to nodes, edges, and connected components; and regional-scale interpretation through aggregation of graph-derived metrics across 20 × 20 km mosaic sub-grid cells alongside model-confidence and image-exposure information.

B. Study Area

This study incorporates three focal landscapes in northern Alaska near the Jago River, Utqiaġvik, and Prudhoe Bay (Fig. 1). The Jago River site in northeastern Alaska represents a more inland tundra setting where widespread ice-wedge degradation and associated changes in microtopography,

hydrology, soils, ground ice, and vegetation have been documented [24]. The Utqiaġvik site is located on the Barrow Peninsula, a low-gradient coastal-plain landscape dominated by ice-wedge polygonal tundra spanning drained thaw-lake basins and interstitial tundra [25]. The Prudhoe Bay site is located within the Prudhoe Bay Oilfield region, an extensive ice-rich permafrost landscape affected by both climate change and infrastructure development [26], [27].

C. Satellite Image Data and Manual Annotation

To reduce ambiguity, we define the terminology used throughout this study as follows. An "image scene" refers to a full-resolution, orthorectified, and pansharpened WorldView-2 raster. Each "tile" is a 2048×2048-pixel (1024×1024 m) sub-array of an image scene that serves as the primary unit for annotation and the subsequent DL analysis. Each 2048×2048-pixel tile (1024×1024 m) was further subdivided into standardized inputs of four sizes: 128×128 pixels (64×64 m), 256×256 pixels (128×128 m), 512×512 pixels (256×256 m), and 1024×1024 pixels (512×512 m). This subdivision enabled systematic evaluation of how varying spatial context influenced model performance.

We acquired high-resolution multispectral satellite imagery from Vantor (formerly Maxar) WorldView satellite series. The selected imagery covers Alaskan tundra landscapes that contain visible TCN expressions. The imagery was provided by the Polar Geospatial Center (PGC) at the University of Minnesota under a National Science Foundation-funded licensing agreement. All images were orthorectified, top-of-atmosphere (TOA) corrected, and pansharpened to a spatial resolution of 0.5 m.

Using a defined annotation protocol, we manually annotated TCN features, including isolated and interconnected polygonal troughs and associated trough-ponds, across 126 image tiles (2048×2048 pixels [1024×1024 m]). These annotations served as reference labels for deep learning (DL) model training and evaluation. The tiles were derived from two WorldView-2 scenes (Table I; Fig. 2). Annotations were conducted at a scale of 1:1000 using a three-band composite comprising NIR2, Red Edge, and Coastal Blue, rendered as false-color RGB. The false-color composite was selected after visual inspection because it provided strong contrast between troughs, ice-wedge polygon interiors, and standing water, facilitating consistent delineation of TCN features across the study sites.

D. Dataset Preparation and Augmentation

The set of 2048×2048-pixel (1024×1024 m) image tiles were partitioned into training (70%), validation (15%), and test (15%) subsets prior to subdivision to prevent pixel-level leakage between subsets. To evaluate the effect of spatial context on DL model performance, each 2048×2048 pixel (1024×1024 m) image tile was further subdivided into four tile sizes: 128×128 pixels (64×64 m), 256×256 pixels (128×128 m), 512×512 pixels (256×256 m), and 1024×1024 pixels (512×512 m). This consistent pixel allocation enabled a fair comparison among all model configurations.

Preprocessing included Contrast Limited Adaptive Histogram Equalization (CLAHE) applied independently at the 2048×2048 (1024×1024 m) image tile level to enhance local contrast and increase model sensitivity to low-relief features. Applying the CLAHE algorithm at this scale ensured that all derived input sizes inherited a fair and consistent transformation. Data augmentation involved random 90° rotations and horizontal/vertical flips, intended to increase overall generalization while preserving the geometry and spatial structure of the underlying TCN.

E. Deep Learning Architectures and Encoders

We compared two major deep learning approaches for semantic segmentation: convolutional neural networks (CNNs) and transformer-based models. For CNNs, we tested five commonly used architectures: U-Net [28], U-Net++ [29], LinkNet [30], PSPNet [31], and MANet [32]. These architectures were chosen to represent a range of design strategies, including encoder-decoder structures, attention mechanisms, and multiscale context aggregation. Each architecture was evaluated using four standard ResNet encoders (ResNet18, ResNet34, ResNet50, and ResNet101) [33], which allowed for consistent comparisons across encoder complexities.

For transformer-based models, we evaluated the SegFormer family using MiT-b0 through MiT-b5 [34]. SegFormer uses a hierarchical encoder allowing multiscale feature modelling while also capturing long-range spatial relationships using self-attention. This is especially relevant for TCNs, which often form long, branching structures across the landscape.

The candidate DL model set was selected to balance diversity of architectures, computational feasibility, and relevance to the type of imagery and target feature being studied. While we did not aim to test every possible architecture, we prioritized models that are well-established in literature, vary in design complexity, and offer a useful baseline for comparing CNNs and ViTs on this task.

F. Deep Learning Model Training

All models were trained using PyTorch [35], utilizing Distributed Data Parallel (DDP) across four NVIDIA Quadro RTX 5000 GPUs in a high-performance computing (HPC) environment of the NSF Texas Advanced Computing Center (TACC) Frontera supercomputer [36]. Training employed the AdamW optimizer [37], learning rate: 0.0001, weight decay: 1e-5), with a Focal loss function, and an effective batch size of four tiles to accommodate memory constraints and early stopping with a patience of 20 epochs evaluated on validation performance. Model selection was based on the validation F1-score, and the held-out test subset was reserved for final reporting.

G. Independent Cross-Site Accuracy Assessment

To evaluate model transferability beyond the initial imagery dataset used for model training, validation, and testing, we conducted an independent pixel-level accuracy assessment at three Alaskan sites near Utqiaġvik, Prudhoe Bay, and the Jago River. The selected best-performing model was applied to 16-

bit Vantor imagery at each site. From the resulting binary prediction masks, we randomly sampled 1,000 pixels classified as TCN and 1,000 pixels classified as background at each site to ensure sufficient representation of the comparatively sparse TCN class. Each sampled pixel was then manually assigned a reference class based on the visible expression in the corresponding Vantor imagery. Precision, recall, and F1-score were calculated from the resulting 2,000-pixel validation sample at each site to evaluate model transferability across different landscapes.

H. Graph Analysis

Binary TCN masks generated by the selected best-performing model were skeletonized to produce a one-pixel centerline representation of the mapped TCN features [38]. These centerline representations were then converted into a graph structure as networks composed of nodes representing junctions or endpoints, and edges representing linear connections between the nodes. Components represent discrete networks in which all nodes and edges are linked but disconnected from other sub-networks. This abstraction allowed us to quantitatively characterize TCN structure using structural and hydrologically relevant metrics, capturing variation in spatial organization and network structure.

We adopt a graph-theoretic framework because the defining property of tundra capillary networks is connectivity. Table 3 summarizes the graph-theoretic metrics that translate connectivity into measurable structural characteristics beyond what pixel- or object-based approaches can provide. DDP and high-memory nodes (HPC Frontera) enabled the scalable implementation of the methodological workflow.

I. Northern Alaska Vantor Mosaic Data Structure and Model Deployment

We used a pre-existing 8-band, 16-bit pansharpened mosaic covering the tundra regions of Alaska, generated from Vantor WorldView-2 and WorldView-3 imagery and compiled by the Polar Geospatial Center (PGC), University of Minnesota. The source imagery was acquired across multiple years, primarily during months that are typically snow-free (June-August), although acquisition times do vary across the mosaic. As a result, the mosaic should be interpreted as a composite of the best available imagery rather than a temporally uniform snapshot.

The PGC prioritized source scenes with limited cloud cover and summer acquisition dates. Where suitable summer imagery was not available, lower-cloud-cover imagery from outside of the preferred seasonal window was used to create a more spatially complete mosaic. Consequently, portions of the mosaic contain some snow, ice, and cloud obstructions that can reduce the visible expression of TCN. The mosaic follows a nested PGC tile scheme, with 100 x 100 km grid cells which are subdivided into 25 individual 20 x 20 km sub-grid cells. The regional mosaic overall comprises 1,821 sub-grid cells corresponding to a footprint of 728,400 km2 and a total file size of approximately 46 TB. This structure provides manageable computational units for model deployment and aggregation of results.

In terrain-mapping applications, the degree of ground exposure visible in imagery plays a critical role in model detection accuracy. Cloud cover and snow presence in early or late-season acquisitions can substantially degrade mosaic quality. To support further interpretation of these effects, we developed a composite quality metric (Fig. 6) that integrates acquisition month and spatial coverage to quantitatively report the suitability of individual mosaic grid cells for TCN detection. This metric characterizes input-image suitability supporting transparent interpretation of regional outputs.

The model was applied independently to each 20 x 20 km mosaic sub-grid cell, by sub-grid across the mosaic, with outputs post-processed to generate binary TCN masks. Although the mosaic was provided as an 8 band product, the regional inferencing process used the same NIR2, Red Edge, and Coastal Blue bands used for model development. These masks were then skeletonized and converted into graph representations for subsequent network analysis. All outputs were georeferenced and reassembled, enabling quantification of TCN structure across the Alaska tundra landscape. The final regional data product was organized at the 20 × 20 km mosaic sub-grid scale. For each sub-grid cell, archived outputs include georeferenced TCN detection masks, post-processed vector representations, skeletonized centerlines, graph-derived node and edge products, and tabular summaries of network metrics. To support interpretation of regional variability, the product also includes model-confidence information and image-exposure metadata describing mosaic suitability, including acquisition timing and spatial coverage. These ancillary layers allow users to distinguish areas of low mapped TCN abundance from areas where snow, cloud, seasonal timing, or incomplete imagery may reduce feature visibility. The final products are available through the Arctic Data Center as Pan-Alaska permafrost tundra capillary network detection and graph theoretic analysis from <1 meter resolution satellite imagery (2011–2025) [45]. Regional production required processing approximately 46 TB of source imagery, generating 49 GB of raster masks and approximately 2.2 TB of GeoPackage/vector and graph products. Excluding model training, mask generation required approximately 3,000 service units on Frontera RTX GPU nodes, while vectorization, graph construction, and packaging required approximately 48,000 service units on Frontera NVDIMM CPU nodes.

III. RESULTS

Across the evaluated CNN model configurations, segmentation performance varied substantially with architecture, encoder, and tile size (Fig. 4) F1-scores ranged from approximately 0.35 to 0.87. U-Net++ with a ResNet50 encoder and 512 x 512 pixel tile inputs achieved the highest CNN performance (F1 = ~0.87). Across the configurations, F1-score ranged from approximately 0.6 to 0.8 for LinkNet; 0.49 to 0.87 for MANet, 0.35 to 0.68 for PSPNet, 0.46 to 0.87 for U-Net, and 0.83 to 0.87 for U-Net++.

The CNN segmentation performance also varied across

encoder and tile-size configurations of ResNet50 produced the highest median F1-score among the tested encoders, while ResNet101 had the widest range of values. Median CNN F1-scores were approximately 0.74 at 128-pixel tile size, 0.82 at 256-pixel tile size, 0.84 at both 512-and-1024-pixel tile size.

SegFormer F1-scores ranged from approximately 0.85 to 0.89 across the evaluated encoder and tile-size configurations (Fig. 4). Median F1 scores were approximately 0.86, 0.89, 0.88 and 0.89 for the 128-, 256-, 512-, and 1024-pixel input tile sizes respectively. Across the encoders median F1-scores ranged from 0.87 to 0.88. with the MiT-b3 encoder at 1024 px achieving the highest overall (0.89).

The selected best-performing SegFormer model (MiT-b3, 1024 px) was evaluated at three independent Alaskan sites: Prudhoe Bay, Utqiaġvik, and Jago. (Fig. 5). Pixel-level precision, recall and F1-score varied across sites. Utqiaġvik achieved the highest pixel-level F1-score (0.93; precision = 0.92; recall = 0.94), followed by Prudhoe Bay (F1 = 0.86; precision = 0.95; recall = 0.78) and the Jago River site (F1 = 0.80; precision = 0.97; recall = 0.68).

The selected best-performing SegFormer model was deployed across the 728,400 km2 northern Alaskan mosaic. Across the analyzed sub-grid cells, the framework mapped approximately 2.7 million km of TCN, represented as approximately 5×10^8 connected components comprising 5.5×10^9 nodes and 5.1×10^9 edges. Graph-theoretic metrics varied across the analyzed sub-grid cells (Figs. 7-9). Node counts ranged from nearly zero to over 30 million per sub-grid cell, with a median of approximately 2 million. Edge counts reached approximately 34 million, with a median of 1.8 million. End-node counts reached approximately 3.6 million, with a median of approximately 500,000. Average node degree had a median of approximately 1.8, while the average edge length ranged from approximately 1.3 to 6.5 m. The number of components ranged from fewer than 500,000, to more than 1.5 million components. Total TCN length ranged from below 5,000 to over 25,000 km per sub-grid cell.

IV. DISCUSSION

This study establishes a scalable segmentation-to-graph framework for mapping TCNs directly from VHSR satellite imagery. The core contribution goes beyond automated delineation of visible TCN expressions to convert those detections into graph-based representations allowing consistent characterization and comparison of this emerging feature across space and time. This systematic evaluation demonstrates that effective TCN mapping requires more than selecting a high-performing segmentation architecture; it requires balancing model design, encoder capacity, and spatial context to detect narrow, spatially continuous features whose visual expression depends on both local spectral-textural patterns and broader permafrost terrain. Applied across a ~730,000 km2 northern Alaska mosaic, the resulting products provide a regional baseline of potential TCN extent and TCN system variability.

The ablation experimentation shows that both architectural and spatial context (tile size) influence TCN segmentation performance. SegFormer MiT-b3 with 1024 x 1024-pixel tile input achieved the highest overall F1-score (0.89), while U-Net++ with a ResNet50 encoder and 512 x 512-pixel tile input achieved the highest CNN performance (0.87). The F1-score difference between the best-performing CNN and Transformer configurations was small. Overall SegFormer family produced a much narrower range of F1-scores across encoder and tile size configurations. The lowest median F1-scores occurred at the smallest input size for both computer vision families, consistent with the importance of spatial context when delineating subtle geomorphologic features [21], [39]. Similar architecture-dependent effects of tile size have been observed in road segmentation, another narrow and spatially continuous feature [21]. They found that both tile size, and its interaction with model architecture, significantly affected performance, with the larger contextual windows producing more coherent feature representations generally. This pattern also reinforces that input extent should be evaluated empirically rather than treated as a secondary implementation choice [21]. Similar improvements from transformer-based representation have been reported in remote-sensing tasks where broader spatial relationships contribute to greater feature discrimination [40]. However, our study cannot establish the superiority of all transformer architectures for this task as it only identifies SegFormer as a highly effective and computationally practical model family for this specific feature detection problem.

The independent pixel-level accuracy assessment further indicates that the selected SegFormer configuration transferred beyond the imagery used for model development. Pixel-level F1-score was highest near Utqiaġvik (0.93), followed by Prudhoe Bay (0.86) and the Jago River site (0.80). Precision remained high across all three sites, while recall varied more substantially. The cross-site pattern therefore indicates that omission errors are a more important limitation than false detections when the model is applied across differing tundra landscapes. This result is consistent with the broader difficulty of mapping Arctic land-surface features across environments that vary in vegetation, wetness, microtopography, seasonal state, and image contrast [2], [12], [15]. It also reinforces the importance of expanding reference datasets beyond a single development region. Additional annotations spanning a wider range of terrain settings and acquisition conditions may improve recall while preserving the high precision observed across the independent sites.

Graph theory expands the possible analytical value of the regional product. This work moves beyond raster masks to organize the mapped TCN features into graph theory networks. The workflow provides a consistent and scalable framework for measuring the organization of the features across space and time. Prior studies have shown that ice-wedge degradation can reorganize surface-water pathways and alter landscape drainage structure [2], [12], [41]. Graph-derived metrics therefore provide a useful lens for comparing TCN systems across landscapes. Despite this their interpretation should remain constrained, they describe geometry and connectivity of visible surface expressions only. They are not direct measurements of hydrology or developmental stage of the polygonal terrain. Establishing a process-based interpretation approach will require comparison with rich data sources including field observation, hydrological and biogeochemical measurements, and very-high resolution elevation data.

Regional deployment further demonstrates the practical value of the segmentation-to-graph workflow. Across 1,821 sub-grid cells, the model mapped and generated graph-theoretic summaries for approximately 2.7 million km of TCN. This work provides a quantitative baseline for examining where visible TCN are concentrated, as well as whether they are sparser, or more connected. The produced dataset should not be treated as a definitive classification of hydrological state, instead it should be treated as a regional baseline for the TCN system. Future work should explore the observed patterns in relation to ground-ice conditions, topography, vegetation, geology, surface water, and permafrost degradation. Interpretation of the regional outputs should also account for the characteristics of the source mosaic imagery. The PGC mosaic is multi-year, assembled from the best available satellite observations rather than a temporally uniform product. A multitude of factors including acquisition timing, cloud obstruction, wetness, shadows, and imagery coverage can all impact the visibility of TCN expression. The accompanying mosaic-quality metric provides a proxy for the suitability of the available imagery to allow users to identify areas where regional comparisons should be treated with greater caution.

Several limitations suggest next steps for this work. The annotated dataset was produced from a limited number of scenes, with varying recall performance, but high precision during the independent-site assessment. These results suggest that the mapped TCN extent may be conservative in some landscapes. Expanding the reference dataset across space and time should improve the recall robustness of the model. The transformer ablation benchmark was limited to only the SegFormer family. While the performance was good, additional transformer architectures should be explored for potential segmentation ability increases. Graph theory derived metrics require calibration against both field and elevation measurements to allow them to act as hydrological and geomorphological indicators. Lastly a reliable multi-temporal analysis would elevate the potential of this work, but require explicit controls for imagery timing, ground exposure levels, temporal variability. The current workflow provides a strong foundation for this work, but apparent changes in mapped structure cannot be interpreted as geomorphic change until image-condition can be separated from landscape evolution.

Future vision transformer-based frameworks could extend beyond image-based inputs; embeddings for location, seasonality, and terrain can help constrain predictions in geomorphologically diverse regions, improving both transferability and interpretability. Recent advances illustrate this potential: SatClip [42] learns location embeddings that generalize across environmental gradients; Prithvi-EO [43] utilizes large-scale pretraining to integrate spatial and temporal context; AlphaEarth [44] integrates multi-modal and temporal embeddings, including climatic and biophysical variables, and VitDetLoc [40] demonstrates that location aware ViTs improve segmentation performance in Arctic remote sensing contexts. Embedding-rich transformer architectures therefore offer a promising path forward for understanding large scale landscape changes.

This study provides a reproducible framework for mapping visible TCN expression across northern Alaska. The resulting products move beyond feature detection alone, providing information about network structure at a scale that can not be achieved through field surveys or manual delineation. This framework provides a foundation for future studies to examine how the organization of fine-scale drainage vary across degrading permafrost regions, and how those structural patterns relate to broader Arctic hydrological change and landscape evolution.

V. Conclusion

This study presents a scalable GeoAI segmentation-to-graph framework for mapping visible TCN expressions directly from VHSR satellite imagery. The framework integrates spatial-context-aware image segmentation, systematic model evaluation, graph construction, and regional-scale interpretation into a coherent workflow for transforming large image mosaics into interpretable landscape products. The systematic ablation evaluation supported the use of SegFormer MiT-b3 with 1024 x 1024-pixel inputs as the highest performing model configuration. Independent pixel-level accuracy assessment supported the application of the selected model beyond the model development imagery. By converting image-based segmentation outputs into nodes, edges, connected components, and regional network metrics, the workflow enables characterization of TCN extent, connectivity, spatial organization, and structural variability across northern Alaska. Deployed across a 728,400 km2 northern Alaska mosaic, the framework mapped approximately 2.7 million km of TCN and generated graph-theoretic summaries for 1,821 20 x 20 km sub-grid cells. The resulting product provides the first regional baseline for visible TCN expressions across northern Alaska and demonstrates a transferable GeoAI framework for converting VHSR Earth-observation imagery into interpretable graph-based landscape products through the integration of deep learning, spatial-context modeling, and network analysis.

Figures:

Figure 1 Circum-Arctic permafrost extent [cite] and northern Alaska study-region context. Permafrost extent classes are shown across the Arctic, with the circumpolar tree line shown in green and the Vantor WorldView-2/3 mosaic footprint outlined in black. Letters indicate the three focal landscapes used in this study: Jago River (A), Prudhoe Bay (B), and Utqiaġvik (C).

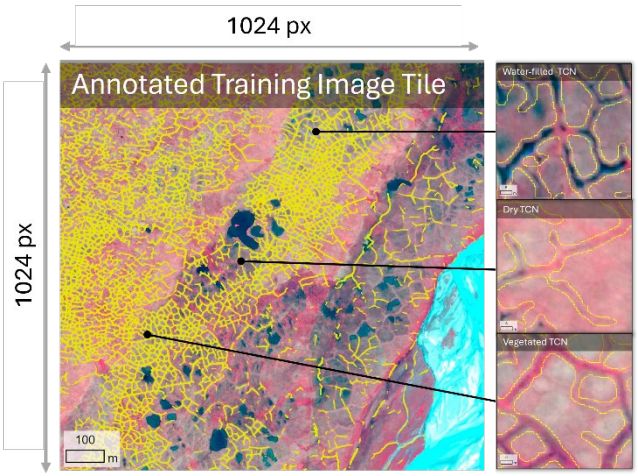

Figure 2 Example annotated training tile and representative TCN surface expressions. The main panel shows a 512 × 512 m image tile, equivalent to 1024 × 1024 pixels at 0.5 m spatial resolution, from WorldView-2 imagery near the Jago River. The image is displayed as a standard false-color composite, with manually delineated TCN reference labels overlaid in yellow. The inset panels show representative examples of water-filled, dry, and vegetated TCN expressions, illustrating the visual variability included in the annotation dataset.

TABLE I
SUMMARY OF MANUALLY ANNOTATED TCN IMAGE–MASK DATASET

METRIC	VALUE
Total image–mask tile pairs	126 PAIRS
Pixel resolution	0.5 M
Total training area (pixels)	528,487,104 PX
Total training area (km²)	132.12 KM²
Average % of pixels labeled TCN	3.51%
Total TCN length	9,500 KM
Median % labeled	2.45%
Min % labeled	0.00%
Max % labeled	14.18%
Std. deviation (% labeled)	3.10%

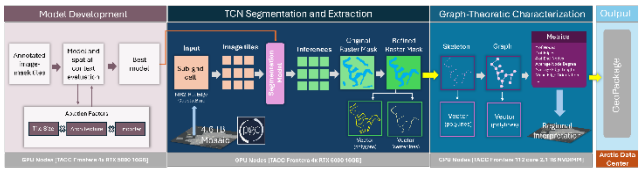

Figure 3 GeoAI segmentation-to-graph framework for regional TCN mapping and graph-theoretic characterization. The workflow links systematic model development, spatial context evaluation, image segmentation, raster mask refinement, vector extraction, graph construction, metric calculation, and regional interpretation. Annotated image-mask tiles were used to evaluate tile size, architecture, and encoder configurations before selecting a deployment model for regional inference. The selected model was applied to 1024 × 1024 pixel image tiles extracted from 20 × 20 km mosaic sub-grid cells to generate TCN raster masks. Refined masks were converted to polygon and centerline vector products, and centerlines were transformed into skeleton and graph representations. Graph-derived metrics, including node counts, edge counts, end-nodes, edge length, edge orientation, and connected components, were summarized to support regional interpretation of TCN extent and structural organization across Arctic near-surface landscapes. Final masks, vectors, graph metrics, and summary products were packaged as GeoPackage outputs for dissemination through the Arctic Data Center.

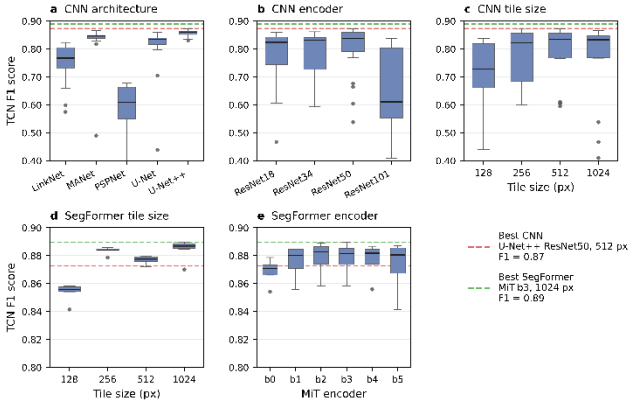

Figure 4 Systematic ablation results for TCN segmentation model development. CNN configurations are summarized by (a) architecture, (b) ResNet encoder, and (c) input tile size. SegFormer configurations are summarized by (d) input tile size and (e) MiT encoder. F1-scores are reported for the held-out test subset, showing the effects of model family, encoder configuration, and spatial context on segmentation performance.

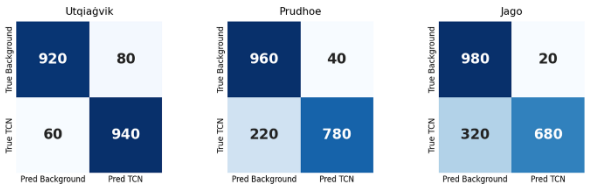

Figure 5 Independent cross-site pixel-level accuracy assessment for the selected SegFormer MiT-b3 model. Confusion matrices show classification results for Utqiaġvik, Prudhoe Bay, and Jago River using 2,000 manually interpreted

validation pixels per site, consisting of 1,000 pixels predicted as TCN and 1,000 pixels predicted as background. Rows indicate reference classes and columns indicate model-predicted classes. The model maintained high precision across all three sites, while TCN omission errors increased from Utqiaġvik to Prudhoe Bay and Jago River.

TABLE II
GRAPH-THEORETIC METRICS USED TO CHARACTERIZE MAPPED TCN STRUCTURE

Metric	Formula	Interpretation
Number of nodes	$\|V\|$	Structural complexity
Number of edges	$\|E\|$	Segment Abundance
Number of end-nodes	$\sum_{v\in V} \mathbf{1}\{\deg(v)=1\}$	Terminal Features
Average node degree	$\frac{2\|E\|}{\|V\|}$	Node linkage
Average edge length	$\frac{1}{\|E\|}\sum_{e\in E}\ell(e)$	Segment scale
Mean edge orientation	$\operatorname{atan2}\left(\sum_{e\in E}\sin\theta_e, \sum_{e\in E}\cos\theta_e\right)$	Directional organization
Number of components	$\|\mathcal{C}(G)\|$	Fragmentation
Average component size	$\frac{1}{\|\mathcal{C}(G)\|}\sum_{C_i\in\mathcal{C}(G)} S(C_i)$	Typical component size
Largest component size	$\max_{C_i\in\mathcal{C}(G)} S(C_i)$	Dominant component size
Total TCN lenngth	$\sum_{e\in E}\ell(e)$	Mapped TCN extent

Note: $(G=(V,E))$, where (V) is the set of nodes and (E) is the set of edges. Edge length is denoted by $(\ell(e))$, edge orientation by (θ_e), and $(\mathcal{C}(G))$ is the set of connected components. Component size is defined as $\left(S(C_i)=\sum_{e\in E(C_i)}\ell(e)\right)$

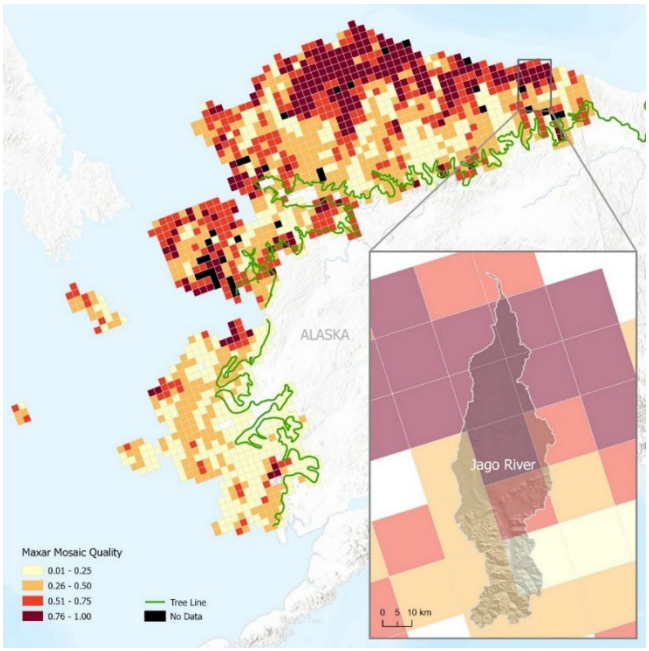

Figure 6 Spatial variation in Vantor WorldView-2/3 mosaic quality across the northern Alaska deployment region. The composite quality metric summarizes the suitability of each 20 × 20 km mosaic sub-grid cell for TCN detection based on image acquisition timing and spatial coverage. Higher values indicate more suitable imagery for detecting visible TCN expressions. The green line indicates the tree line, black cells indicate no data, and the Jago River watershed inset provides a site-scale example within one of the focal study landscapes.

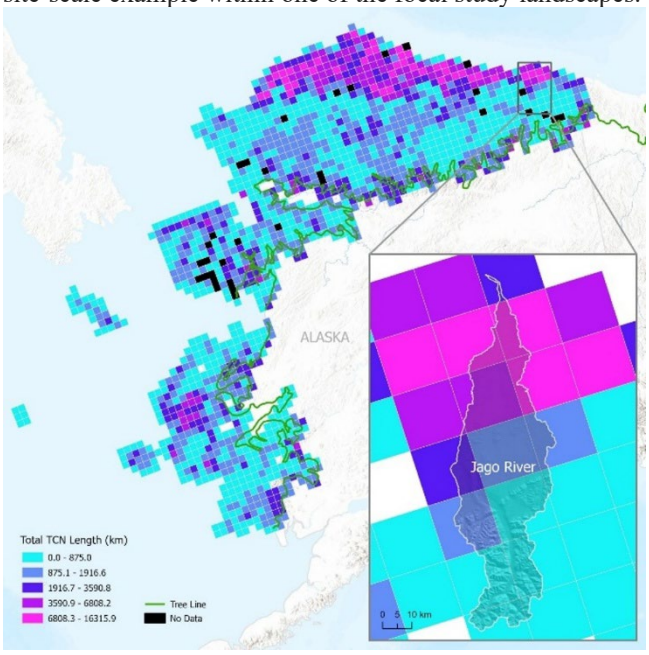

Figure 7 Spatial variation in total mapped TCN length across the northern Alaska deployment region. Values represent the cumulative length of skeletonized TCN centerlines within each 20 × 20 km mosaic sub-grid cell. Higher values indicate greater mapped TCN extent. The green line indicates the tree line, black cells indicate no data, and the Jago River watershed inset provides a site-scale example of regional metric variation within one focal study landscape.

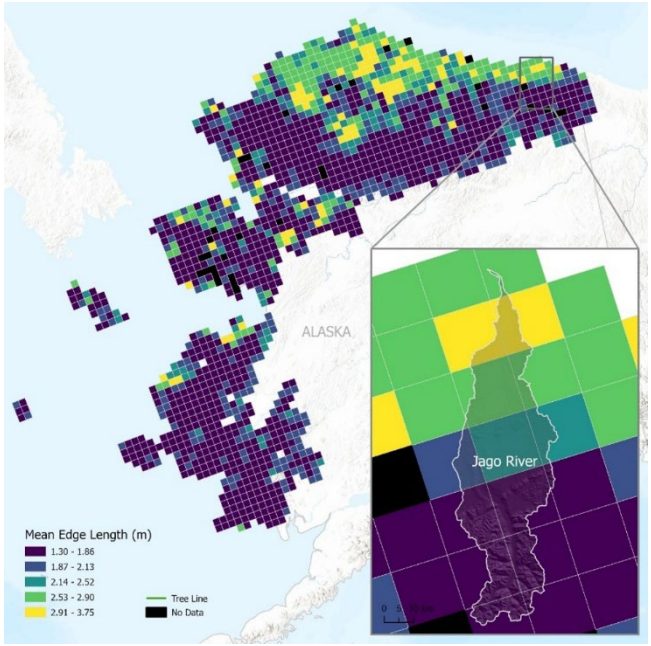

Figure 8 Spatial variation in mean TCN graph-edge length across the northern Alaska deployment region. Values represent the average length of graph edges connecting adjacent nodes within each 20 × 20 km mosaic sub-grid cell. This metric summarizes local segment-scale geometry of the mapped TCN network. The green line indicates the tree line, black cells indicate no data, and the Jago River watershed inset provides a site-scale example of graph-metric variability within one focal study landscape.

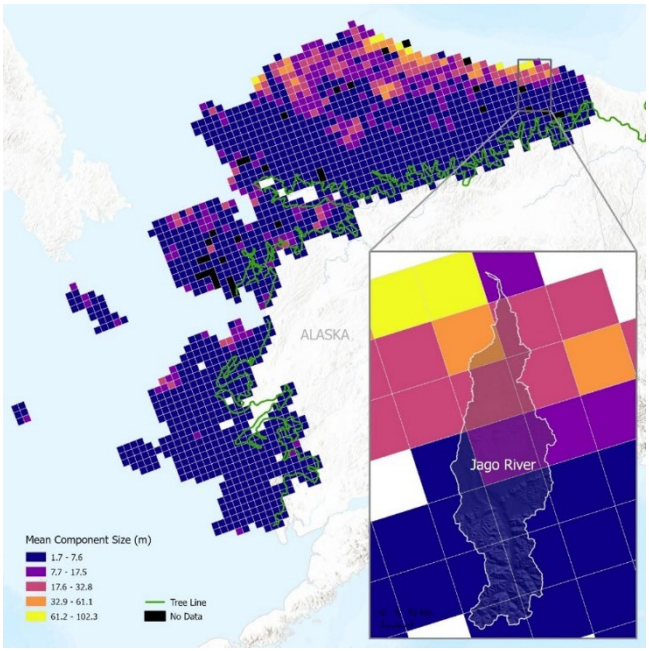

Figure 9 Spatial variation in mean TCN connected-component size across the northern Alaska deployment region. Values represent the average size of discrete connected TCN components within each 20 × 20 km mosaic sub-grid cell. This metric summarizes whether mapped TCN features occur as short, isolated segments or larger connected networks. The green line indicates the tree line, black cells indicate no data, and the Jago River watershed inset provides a site-scale example of connected-network structure within one focal study landscape.

Data Availability:

The Pan-Alaska TCN detection and graph-theoretic analysis products are available through the Arctic Data Center: Pan-Alaska permafrost tundra capillary network detection and graph theoretic analysis from <1 meter resolution satellite imagery (2011–2025), doi.org/10.18739/A2XD0R08N [45]. The archived dataset includes georeferenced detection masks, vectorized TCN products, skeletonized centerline products, graph-theoretic metrics summarized by 20 × 20 km mosaic sub-grid cell, model-confidence information, and image-exposure metadata used to support interpretation of regional output quality.

REFERENCES

[2] M. Rantanen *et al*., "The Arctic has warmed nearly four times faster than the globe since 1979," *Commun. Earth Environ.*, vol. 3, no. 1, Aug. 2022, Art. no. 168, doi: 10.1038/s43247-022-00498-3.

[3] A. K. Liljedahl et al., "Pan-Arctic ice-wedge degradation in warming permafrost and its influence on tundra hydrology," Nat. Geosci., vol. 9, no. 4, pp. 312-318, Apr. 2016, doi: 10.1038/ngeo2674.

[4] J. Obu, "How much of the Earth's surface is underlain by permafrost?," J. Geophys. Res. Earth Surf., vol. 126, no. 5, May 2021, Art. no. e2021JF006123, doi: 10.1029/2021JF006123.

[5] Y. Shur, K. M. Hinkel, and F. E. Nelson, "The transient layer: Implications for geocryology and climate-change science," Permafrost Periglacial Process., vol. 16, no. 1, pp. 5-17, Jan. 2005, doi: 10.1002/ppp.518.

[6] J. Nitzbon et al., "Fast response of cold ice-rich permafrost in northeast Siberia to a warming climate," Nat. Commun., vol. 11, no. 1, May 2020, Art. no. 2201, doi: 10.1038/s41467-020-15725-8.

[7] M. J. Lara et al., "Tundra landform and vegetation productivity trend maps for the Arctic Coastal Plain of northern Alaska," Sci. Data, vol. 5, no. 1, Apr. 2018, Art. no. 180058, doi: 10.1038/sdata.2018.58.
[8] M. J. Lara et al., "Local-scale Arctic tundra heterogeneity affects regional-scale carbon dynamics," Nat. Commun., vol. 11, no. 1, Sep. 2020, Art. no. 4925, doi: 10.1038/s41467-020-18768-z.
[9] R. F. Black, "Ice-wedge polygons of northern Alaska," in Glacial Geomorphology, D. R. Coates, Ed. Dordrecht, The Netherlands: Springer, 1982, doi: 10.1007/978-94-011-6491-7_9.
[10] L. Plug and B. Werner, "Nonlinear dynamics of ice-wedge networks and resulting sensitivity to severe cooling events," Nature, vol. 417, pp. 929-933, Jun. 2002, doi: 10.1038/nature00796.
[11] S. A. Harris et al., Glossary of Permafrost and Related Ground-Ice Terms. Ottawa, ON, Canada: Nat. Res. Council Canada, Assoc. Committee Geotech. Res., Permafrost Subcommittee, 1988, Tech. Memo. ACGR-TM-142, doi: 10.4224/20386561.
[12] N. A. Wales et al., "Understanding the relative importance of vertical and horizontal flow in ice-wedge polygons," Hydrol. Earth Syst. Sci., vol. 24, pp. 1109-1129, Mar. 2020, doi: 10.5194/hess-24-1109-2020.
[13] A. K. Liljedahl, C. Witharana, and E. Manos, "The capillaries of the Arctic tundra," Nat. Water, vol. 2, pp. 611-614, Jul. 2024, doi: 10.1038/s44221-024-00276-9.
[14] T. Rettelbach et al., "A quantitative graph-based approach to monitoring ice-wedge trough dynamics in polygonal permafrost landscapes," Remote Sens., vol. 13, no. 16, Aug. 2021, Art. no. 3098, doi: 10.3390/rs13163098.
[15] C. J. Abolt, M. H. Young, A. L. Atchley, and C. J. Wilson, "Brief communication: Rapid machine-learning-based extraction and measurement of ice wedge polygons in high-resolution digital elevation models," Cryosphere, vol. 13, no. 1, pp. 237-245, Jan. 2019, doi: 10.5194/tc-13-237-2019.
[16] C. Witharana et al., "An object-based approach for mapping tundra ice-wedge polygon troughs from very high spatial resolution optical satellite imagery," Remote Sens., vol. 13, no. 4, Feb. 2021, Art. no. 558, doi: 10.3390/rs13040558.
[17] M. A. E. Bhuiyan, C. Witharana, and A. K. Liljedahl, "Use of very high spatial resolution commercial satellite imagery and deep learning to automatically map ice-wedge polygons across tundra vegetation types," J. Imaging, vol. 6, no. 12, Dec. 2020, Art. no. 137, doi: 10.3390/jimaging6120137.
[18] M. Kanevskiy et al., "Degradation and stabilization of ice wedges: Implications for assessing risk of thermokarst in northern Alaska," Geomorphology, vol. 297, pp. 20-42, Nov. 2017, doi: 10.1016/j.geomorph.2017.09.001.
[19] B. Gao et al., "Automated characterization of yardangs using deep convolutional neural networks," Remote Sens., vol. 13, no. 4, Feb. 2021, Art. no. 733, doi: 10.3390/rs13040733.
[20] M. Barthélemy, "Spatial networks," Phys. Rep., vol. 499, no. 1-3, pp. 1-101, Feb. 2011, doi: 10.1016/j.physrep.2010.11.002.
[21] M. E. J. Newman, "The structure and function of complex networks," SIAM Rev., vol. 45, no. 2, pp. 167-256, Jun. 2003, doi: 10.1137/S003614450342480.
[22] M. T. Jorgenson et al., "Rapid transformation of tundra ecosystems from ice-wedge degradation," Glob. Planet. Change, vol. 216, Sep. 2022, Art. no. 103921, doi: 10.1016/j.gloplacha.2022.103921.
[23] M. J. Lara et al., "Polygonal tundra geomorphological change in response to warming alters future CO2 and CH4 flux on the Barrow Peninsula," Glob. Change Biol., vol. 21, no. 4, pp. 1634-1651, Apr. 2015, doi: 10.1111/gcb.12757.
[24] M. K. Raynolds et al., "Cumulative geoecological effects of 62 years of infrastructure and climate change in ice-rich permafrost landscapes, Prudhoe Bay Oilfield, Alaska," Glob. Change Biol., vol. 20, no. 4, pp. 1211-1224, Apr. 2014, doi: 10.1111/gcb.12500.
[25] M. Kanevskiy et al., "The shifting mosaic of ice-wedge degradation and stabilization in response to infrastructure and climate change, Prudhoe Bay Oilfield, Alaska, USA," Arctic Sci., vol. 8, no. 2, pp. 498-530, Jun. 2022, doi: 10.1139/as-2021-0024.
[26] E. D. Hafner, P. Barton, R. C. Daudt, J. D. Wegner, K. Schindler, and Y. Bühler, "Automated avalanche mapping from SPOT 6/7 satellite imagery with deep learning: Results, evaluation, potential and limitations," Cryosphere, vol. 16, no. 9, pp. 3517-3530, Sep. 2022, doi: 10.5194/tc-16-3517-2022.
[27] K. Nogueira, M. Dalla Mura, J. Chanussot, W. R. Schwartz, and J. A. dos Santos, "Dynamic multicontext segmentation of remote sensing images based on convolutional networks," IEEE Trans. Geosci. Remote Sens., vol. 57, no. 10, pp. 7503-7520, Oct. 2019, doi: 10.1109/TGRS.2019.2913861.
[28] C.-I. Cira, M.-Á. Manso-Callejo, R. Alcarria, T. Iturrioz, and J.-J. Arranz-Justel, "Insights into the effects of tile size and tile overlap levels on semantic segmentation models trained for road surface area extraction from aerial orthophotography," Remote Sens., vol. 16, no. 16, Aug. 2024, Art. no. 2954, doi: 10.3390/rs16162954.
[29] O. Ronneberger, P. Fischer, and T. Brox, "U-Net: Convolutional networks for biomedical image segmentation," in Proc. Med. Image Comput. Comput.-Assist. Intervention, Munich, Germany, 2015, pp. 234-241, doi: 10.1007/978-3-319-24574-4_28.
[30] Z. Zhou, M. M. Rahman Siddiquee, N. Tajbakhsh, and J. Liang, "UNet++: A nested U-Net architecture for medical image segmentation," in Deep Learning in Medical Image Analysis and Multimodal Learning for Clinical Decision Support, D. Stoyanov et al., Eds. Cham, Switzerland: Springer, 2018, pp. 3-11, doi: 10.1007/978-3-030-00889-5_1.
[31] A. Chaurasia and E. Culurciello, "LinkNet: Exploiting encoder representations for efficient semantic segmentation," in Proc. IEEE Vis. Commun. Image Process. (VCIP), St. Petersburg, FL, USA, 2017, pp. 1-4, doi: 10.1109/VCIP.2017.8305148.
[32] H. Zhao, J. Shi, X. Qi, X. Wang, and J. Jia, "Pyramid scene parsing network," in Proc. IEEE Conf. Comput. Vis. Pattern Recognit. (CVPR), Honolulu, HI, USA, 2017, pp. 6230-6239, doi: 10.1109/CVPR.2017.660.
[33] R. Li et al., "Multiattention network for semantic segmentation of fine-resolution remote sensing images," IEEE Trans. Geosci. Remote Sens., vol. 60, pp. 1-13, 2022, Art. no. 5607713, doi: 10.1109/TGRS.2021.3093977.
[34] K. He, X. Zhang, S. Ren, and J. Sun, "Deep residual learning for image recognition," in Proc. IEEE Conf. Comput. Vis. Pattern Recognit. (CVPR), Las Vegas, NV, USA, 2016, pp. 770-778, doi: 10.1109/CVPR.2016.90.
[35] E. Xie, W. Wang, Z. Yu, A. Anandkumar, J. M. Alvarez, and P. Luo, "SegFormer: Simple and efficient design for semantic segmentation with transformers," arXiv:2105.15203, 2021. [Online]. Available: https://arxiv.org/abs/2105.15203
[36] A. Paszke et al., "PyTorch: An imperative style, high-performance deep learning library," arXiv:1912.01703, 2019. [Online]. Available: https://arxiv.org/abs/1912.01703
[37] D. Stanzione et al., "Frontera: The evolution of leadership computing at the National Science Foundation," in Proc. Practice Exp. Adv. Res. Comput. (PEARC), Portland, OR, USA, 2020, pp. 106-111, doi: 10.1145/3311790.3396656.
[38] I. Loshchilov and F. Hutter, "Decoupled weight decay regularization," arXiv:1711.05101, 2019. [Online]. Available: https://arxiv.org/abs/1711.05101
[39] S. van der Walt et al., "scikit-image: Image processing in Python," PeerJ, vol. 2, Jun. 2014, Art. no. e453, doi: 10.7717/peerj.453.
[40] L. P. Soares, H. C. Dias, G. P. B. Garcia, and C. H. Grohmann, "Landslide segmentation with deep learning: Evaluating model generalization in rainfall-induced landslides in Brazil," Remote Sens., vol. 14, no. 9, May 2022, Art. no. 2237, doi: 10.3390/rs14092237.
[41] A. S. Perera et al., "Pan-Arctic permafrost landform and human-built infrastructure feature detection with vision transformers and location embeddings," IEEE J. Sel. Topics Appl. Earth Observ. Remote Sens., vol. 19, pp. 7858-7879, 2026, doi: 10.1109/JSTARS.2025.3648673.
[42] M. A. Walvoord and B. L. Kurylyk, "Hydrologic impacts of thawing permafrost: A review," Vadose Zone J., vol. 15, no. 6, pp. 1-20, Jun. 2016, doi: 10.2136/vzj2016.01.0010.
[43] K. Klemmer, E. Rolf, C. Robinson, L. Mackey, and M. Rußwurm, "SatCLIP: Global, general-purpose location embeddings with satellite imagery," Proc. AAAI Conf. Artif. Intell., vol. 39, no. 4, pp. 4347-4355, Apr. 2025, doi: 10.1609/aaai.v39i4.32457.
[44] D. Szwarcman et al., "Prithvi-EO-2.0: A versatile multi-temporal foundation model for Earth observation applications," arXiv:2412.02732, 2024. [Online]. Available: https://arxiv.org/abs/2412.02732
[45] C. F. Brown et al., "AlphaEarth foundations: An embedding field model for accurate and efficient global mapping from sparse label data," arXiv:2507.22291, 2025. [Online]. Available: https://arxiv.org/abs/2507.22291
[46] M. Pimenta, C. Witharana, A. S. Perera, and A. K. Liljedahl, "Pan-Alaska permafrost tundra capillary network detection and graph theoretic analysis from <1 meter resolution satellite imagery (2011–2025)," Arctic Data Center, 2026, doi.org/10.18739/A2XD0R08N.